Supporting information

Anisotropic Growth of ZnO Nanoparticles Driven by the Structure of Amine Surfactants: The Surface Dynamic on Nanocrystal Rules

Yinping Wang,[a, b] Yannick Coppel,[a] Christine Lepetit,[a] Jean-Daniel Marty,[b] Christophe Mingotaud,[b]* and Myrtil L. Kahn,[a]*

2D plot analysis and multivariate analysis.

2D plot analysis. Each particle is characterized by two sizes, noted D1 and D2, measured on perpendicular axes. These two sizes generally correspond to the length and width of the nano-objects. For each particle and on a same graph, we plot D1 as a function of D2 and also D2 as a function of D1. The aspect ratio of the particle (noted AR) is defined as the ratio between the two lengths AR=D1/D2 (with D1>D2). It is related to a theta angle through the equation AR=tan θ. Higher anisotropy in the shape of a particle corresponds to higher AR value and to a theta angle closer to 90° in the proposed 2D plot. 2D plots present point clouds whose structures can be the result of different sub-populations. To identify these sub-populations, a multivariate analysis was performed with the MIXMOD software (http://mixmod.org) using R package. Apart from the Gaussian character of the probability densities, no assumption about the orientation, shape, and volume of the different sub-populations was made during calculation. The number of sub-populations that composed the point clouds was fixed by the user or chosen numerically thanks to the BIC criteria (Bayesian Information Criterion). Each sub-population was then characterized by the mean of the two studied variables (i.e., short and long axis lengths), as well as the corresponding standard deviations. Additionally, the correlation parameter ρ between both variables was calculated. The correlation is equal to zero when the two variables are totally independent and equal to 1 when they are affinely related to each other.

MIXMOD software

The main purpose of the MIXMOD software (http ://www.mixmod.org) is to discover group structures in multivariate data sets. It is an exploratory data analysis tool for solving clustering and classification problems. Mathematically speaking, for quantitative multivariate data, the MIXMOD software modelises the probability density of the data $x_i = (x_i^1, \cdots, x_i^d)^T$, $i = 1, \cdots, N$ by a mixture f of K multivariate Gaussian densities $h_1, \cdots, h_K$:

$$f(x_i, K, (\mu_k, p_k, \Sigma_k)_{k=1,\cdots,K}) = \sum_{k=1}^{K} p_k h_k(x_i, \mu_k, \Sigma_k) \tag{1}$$

where :

$$h_k(x_i, \mu_k, \Sigma_k) = \frac{1}{\sqrt{2\pi}^d \sqrt{|\Sigma_k|}} \exp\left(-\frac{1}{2}(x_i - \mu_k)^T \Sigma_k^{-1}(x_i - \mu_k)\right)$$

h_k is caracterized by a mean vector μ_k and a variance-covariance matrix Σ_k. $|\Sigma_k|$ denotes the determinant of Σ_k. The estimation of the parameters μ_k, p_k, Σ_k for $k = 1, \cdots, K$ is done by an EM (Expectation-Maximization) algorithm. The aim of this algorithm is to find the "best", the "most likely" estimators of the parameters μ_k, p_k, Σ_k for $k = 1, \cdots, K$ that is to say the estimators that maximize the likelihood :

$$\prod_{i=1}^{N} f(x_i, K, (\mu_k, p_k, \Sigma_k)_{k=1,\cdots,K})$$

This algorithm consists in calculating iteratively until convergence :

$$\alpha_{ik}^{(n)} = \frac{p_k^{(n)} h_k(x_i, \mu_k^{(n)}, \Sigma_k^{(n)})}{\sum_{k=1}^{K} p_k^{(n)} h_k(x_i, \mu_k^{(n)}, \Sigma_k^{(n)})}$$

$$\mu_k^{(n+1)} = \left(\sum_{i=1}^{N} x_i \alpha_{ik}^{(n)}\right) / \left(\sum_{i=1}^{N} \alpha_{ik}^{(n)}\right)$$

$$\Sigma_k^{(n+1)} = \left(\sum_{i=1}^{N} \alpha_{ik}^{(n)} (x_i - \mu_k^{(n)})^T (x_i - \mu_k^{(n)})\right) / \left(\sum_{i=1}^{N} \alpha_{ik}^{(n)}\right)$$

$$p_k^{n+1} = \left(\sum_{i=1}^{N} \alpha_{ik}^{(n)}\right) / N$$

When the estimators $\hat{\mu}_k$, $\hat{p}_k$, $\hat{\Sigma}_k$ for $k = 1, \cdots, K$ are found ; each observation x_i is affected to its "most likely" component $\hat{k}_i$:

$$\hat{k}_i = \text{argmax}_k \frac{\hat{p}_k h_k(x_i, \hat{\mu}_k, \hat{\Sigma}_k)}{\sum_{k=1}^{K} \hat{p}_k h_k(x_i, \hat{\mu}_k, \hat{\Sigma}_k)}$$

Thus a classification in K classes is obtained.
For each K we can calculate $\hat{\mu}_k$, $\hat{p}_k$, $\hat{\Sigma}_k$ for $k = 1, \cdots, K$. To estimate K we choose a model (1) that fits well the data but without too many parameters. For that we choose K that minimizes the BIC (Bayesian Information Criterion) criterion :

$$\hat{K} = \text{argmin}_K \text{BIC}(K) = \text{argmin}_K(-2\ln \prod_{i=1}^{N} f(x_i, K, (\hat{\mu}_k, \hat{p}_k, \hat{\Sigma}_k)_{k=1,\cdots,K}) + \nu_K \ln(N))$$

where ν_K is the number of free parameters in the mixture model with K components.

Statistical indices

The mean vector of a data set $x_i = (x_i^1, \cdots, x_i^d)^T$, $i = 1, \cdots, N$ is estimated by

$$\bar{x} = \frac{1}{N} \sum_{i=1}^{N} x_i.$$

The variance is estimated by

$$\hat{\text{Var}}(x) = \frac{1}{N-1} \sum_{i=1}^{N} (x_i - \bar{x})^2$$

The standard deviation is defined as the square root of the variance. The covariance between two real variables x^1 and x^2 is estimated by

$$\hat{\text{Cov}}(x^1, x^2) = \frac{1}{N-1} \sum_{i=1}^{N} (x_i^1 - \bar{x^1})(x_i^2 - \bar{x^2}).$$

The correlation between x^1 and x^2 is estimated by

$$\hat{\rho}(x^1, x^2) = \frac{\hat{\text{Cov}}(x^1, x^2)}{\sqrt{\hat{\text{Var}}(x^1)}\sqrt{\hat{\text{Var}}(x^2)}}$$

The correlation is equal to zero between two independent variables and equal to 1 between two identical variables.

Modified mixmod software

In the modified version of the MIXMOD software we assume that the first component of the mixture (1) is known. Thus the probability density of the data $x_i = (x_i^1, \cdots, x_i^d)^T$, $i = 1, \cdots, N$ is a mixture f of K multivariate Gaussian densities $h_1, \cdots, h_K$:

$$f(x_i, K, (\mu_k, p_k, \Sigma_k)_{k=1,\cdots,K}) = \sum_{k=1}^{K} p_k h_k(x_i, \mu_k, \Sigma_k)$$

where only μ_1 and Σ_1 are known. The other parameters are unknown. The points belonging to the first component are chosen in a 5% confidence interval around μ_1. Then the standard MIXMOD software is used to classify the other points and determine the number of classes.

Table S1:

Multivariate analysis of the 2D plots corresponding to the TEM images of the Figure 1 (ZnO NPs versus the nature of the amines) through Rmixmod program (the dispersion is given as twice the standard deviation obtained from calculations).

Nature of the amine	Morphology	Proportion (%)	Length (nm)	Width (nm)	Correlation
C_{12}-NH_2	Nanorods	74	16 ± 7	5.0 ± 0.7	0.02
	Isotropic	26	6.6 ± 1.9	6.6 ± 1.9	1.00
C_{12}-$NH(CH_3)$	Isotropic	100	7.3 ± 1.1	7.3 ± 1.1	0.58
C_{12}-$N(CH_3)_2$	Aggregates	100	-	-	-

Synthesis of ZnO nano-objects.

Note that the hydrolysis reaction take place in a homogeneous media, the mixture of the zinc precursor and the alkylamines leading to a liquid phase.[1]

The crystallographic phase of the obtained ZnO is wurtzite, *i.e.* hexagonal. Such results were obtained by powder X-ray diffraction. The diffractograms display the same pattern in the 15° to 90° Θ range, which corresponds to the hexagonal zincite phase (space group P_{63mc}) regardless of the amine (see Figure S1). When the shape of the nanoparticles corresponds to nanorods, the diffractograms present a narrow half-height width (full width at half maximum, FWHM) of the *002* diffraction line compared to the 100 and 101 diffraction peaks. In contrast, isotropic nanoparticles show no particular narrowness of the *002* diffraction line and similar half-height widths are observed for the *002*, *100*, and *101* diffraction peaks. The small FWHM of the *002* diffraction line observed for the nanorods is in agreement with the existence of a privileged axis of growth – the c axis of the zincite phase for the ZnO nanorods. Estimation of the crystallite size using Debye-Sherrer equation gives values in agreement with TEM size analysis (see Table S2), in agreement with our previously published results stating that the nano-objects obtained following this organometallic approach are indeed monocrystalline.[2]

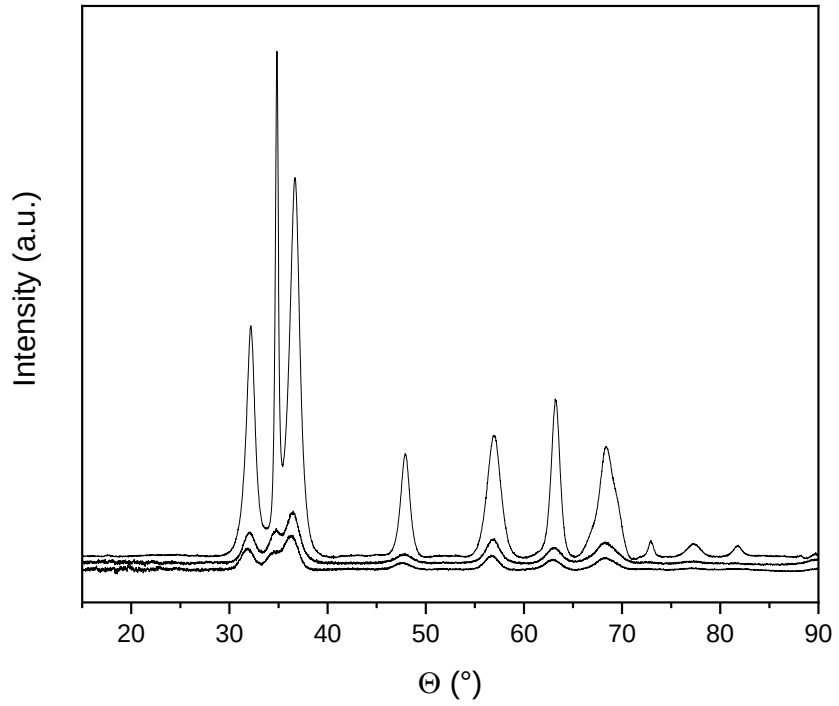

Figure S1: X-ray diffraction pattern recorded at room temperature for ZnO nanoparticles synthesized with C_{12}-NH_2 (top), C_{12}-$NH(CH_3)$ (medium), and C_{12}-$N(CH_3)_2$ (bottom).

Table S2:

Estimation of the crystallite size using Debye-Sherrer equation. Full width at half maximum, FWHM, of ZnO nanoparticles synthesized with C_{12}-NH_2, C_{12}-$NH(CH_3)$, and C_{12}-$N(CH_3)_2$ are reported for *100*, *002*, and *101* peaks.

Sample	100 FWHM	002 FWHM	101 FWHM
ZnO@ C_{12}-NH_2	5	40	5
ZnO@C_{12}-$NH(CH_3)$	6	5	5
ZnO@C_{12}-$N(CH_3)_2$	6	6	5

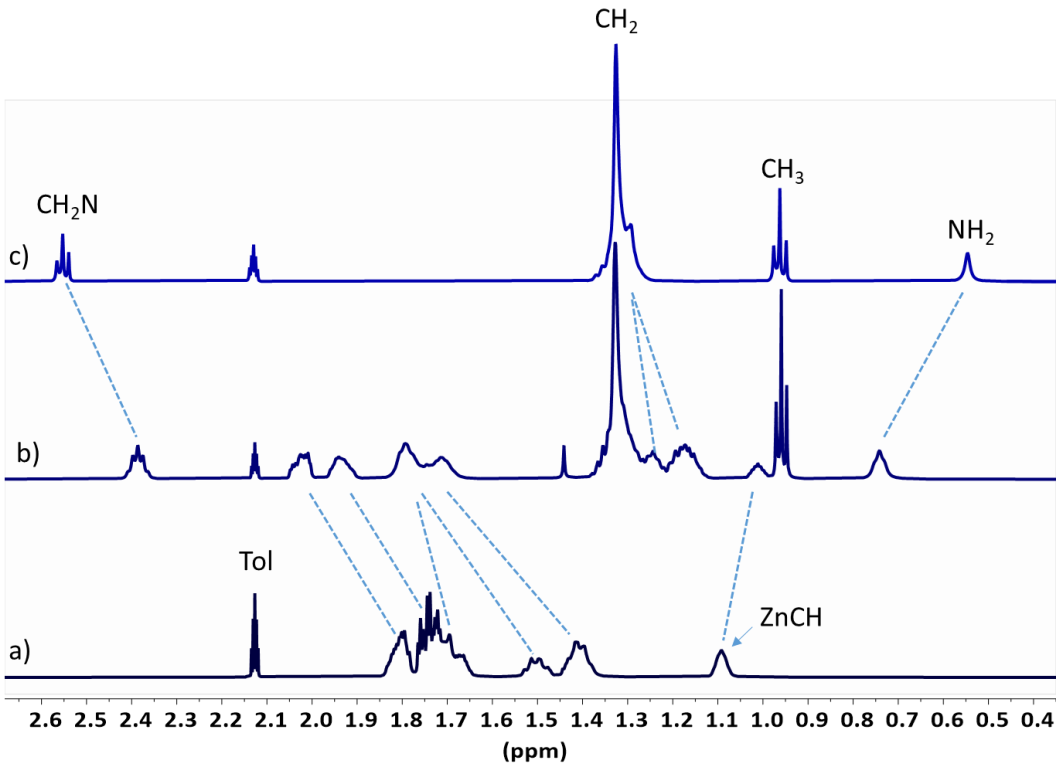

Figure S2: ^{1}H NMR spectra (298 °K, toluene-d_8) of [$ZnCy_2$] (a), of [$ZnCy_2$] with 2 eq. of C_{12}-NH_2 after 1 h of mixing (b) and of C_{12}-NH_2 (c).

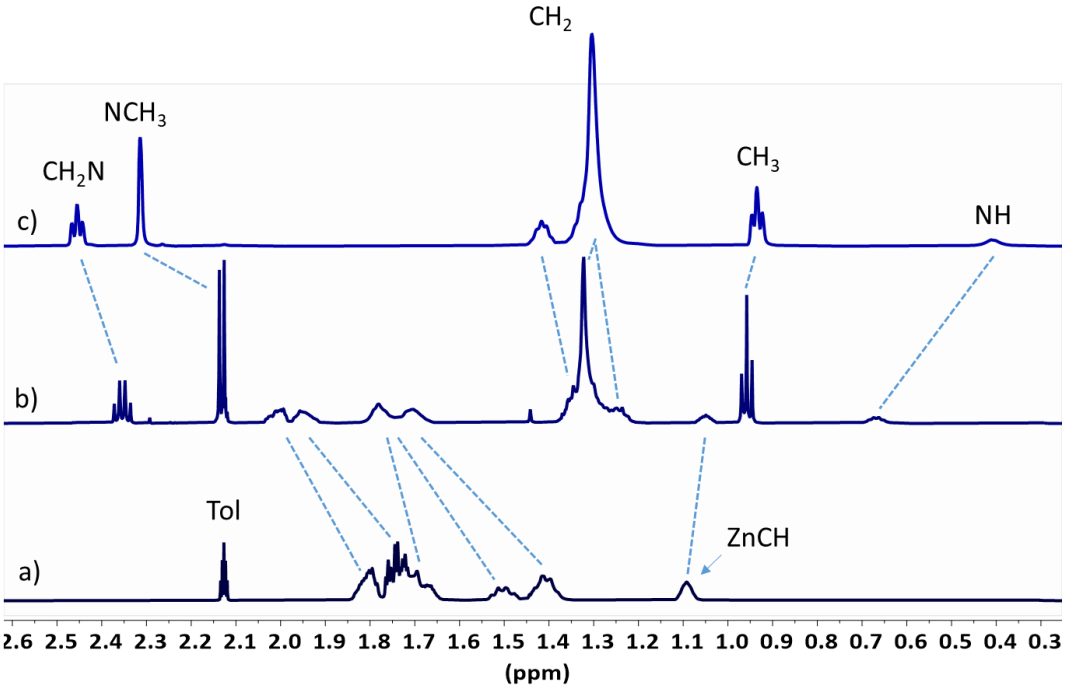

Figure S3: ^{1}H NMR spectra (298 °K, toluene-d_8) of [$ZnCy_2$] (a), of [$ZnCy_2$] with 2 eq. of C_{12}-NH(CH_3) after 1h of mixing (b) and of C_{12}-NH(CH_3) (c).

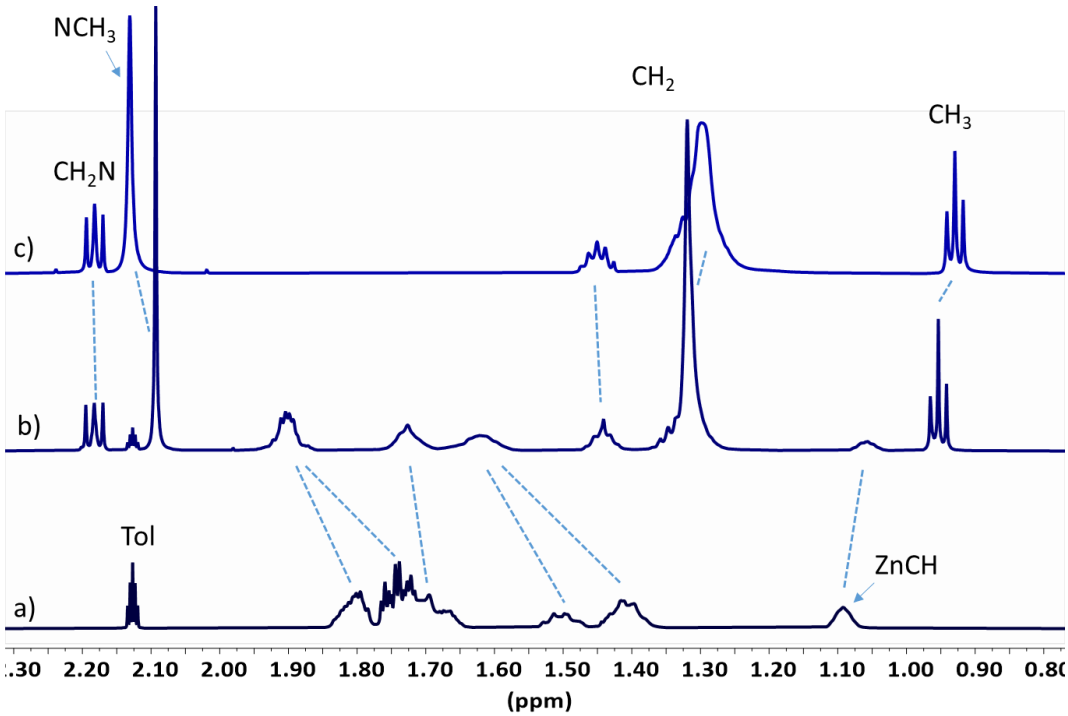

Figure S4: ^{1}H NMR spectra (298 °K, toluene-d_8) of [$ZnCy_2$] (a), of [$ZnCy_2$] with 2 eq. of C_{12}-N(CH_3)$_2$ after 1h of mixing (b) and of C_{12}-N(CH_3)$_2$ (c).

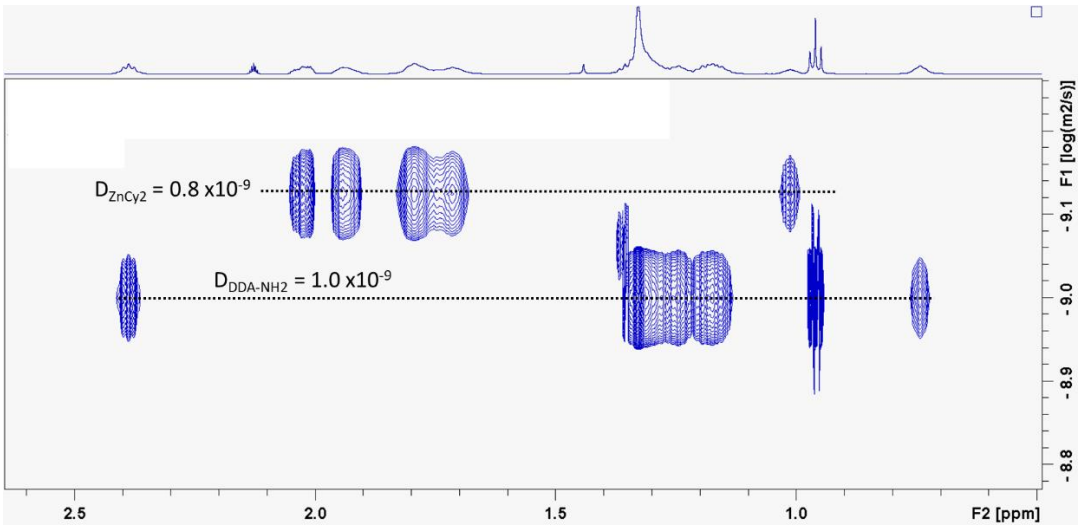

Figure S5: ^{1}H DOSY NMR spectra of [$ZnCy_2$] with 2 eq. of C_{12}-NH_2 after 1h of mixing.

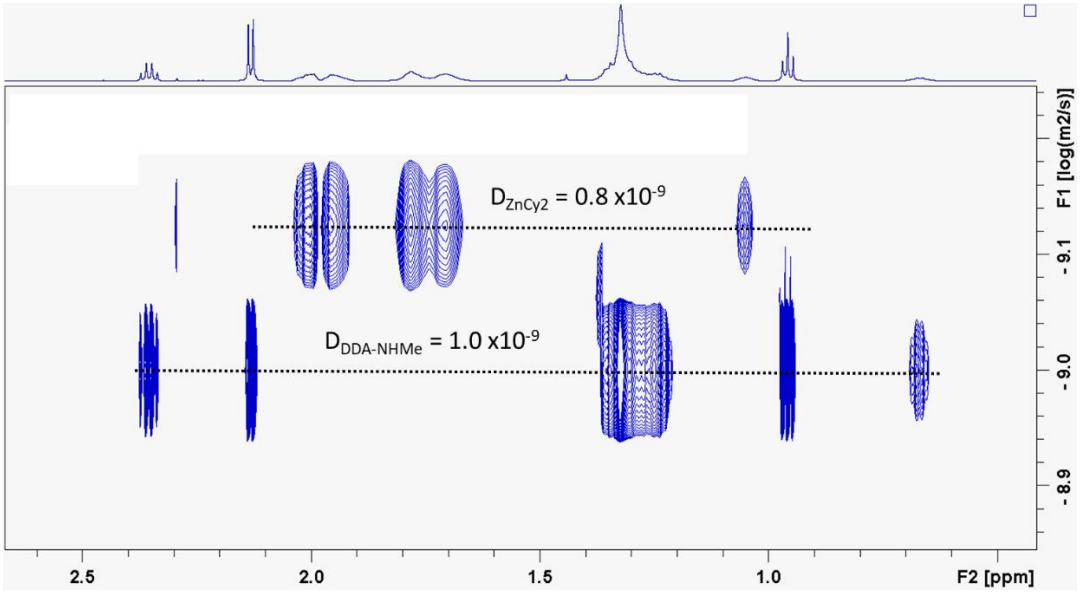

Figure S6: ^{1}H DOSY NMR spectra of [$ZnCy_2$] with 2 eq. of C_{12}-$NH(CH_3)$ after 1h of mixing.

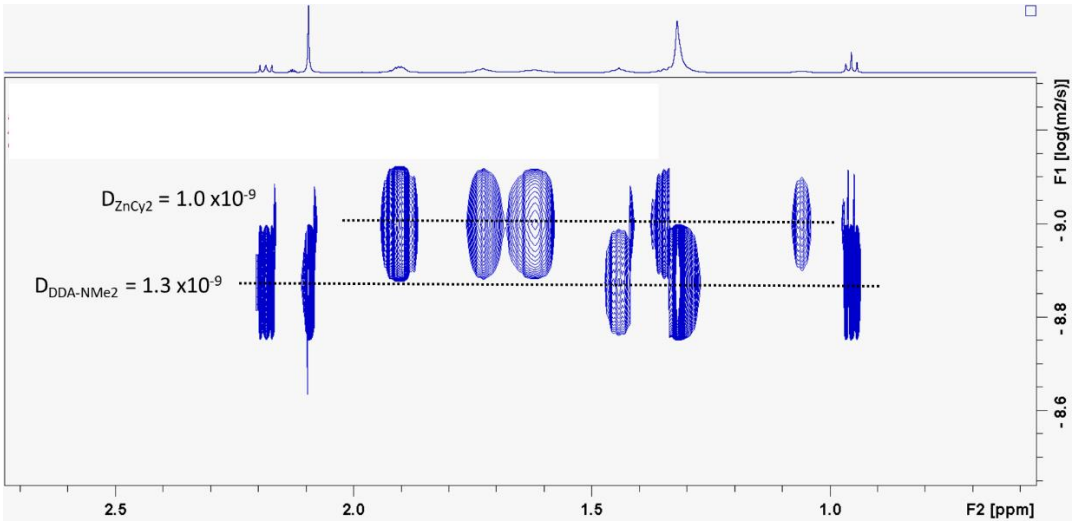

Figure S7: ^{1}H DOSY NMR spectra of [$ZnCy_2$] with 2 eq. of C_{12}-$N(CH_3)_2$ after 1h of mixing.

Table S3: Selected geometrical data of [$ZnCy_2$] and the [$ZnCy_2(C_6H_{13}NH_xMe_{2-x})$] complexes (x = 0 - 2), calculated at the PBE-D3/DGDZVP level. *: PCM calculation in octylamine solvent, ε = 3.1). Distances in Å and angles in degrees.

	Zn-C distance		C-Zn-C angle	H_{axial}-C-C-H_{axial} dihedral	Zn-N distance
[$ZnCy_2$]	1.972	1.972	180	160	-
[$ZnCy_2$]*	1.986	1.986	179	161	-
[$ZnCy_2(C_6H_{13}NH_2)$]	1.999	2.002	158	50	2.345
[$ZnCy_2(C_6H_{13}NH_2)$]*	2.007	2.010	159	50	2.337
[$ZnCy_2(C_6H_{13}NHMe)$]	1.998	2.003	157	84	2.368
[$ZnCy_2(C_6H_{13}NHMe)$]*	2.008	2.013	156	77	2.354
[$ZnCy_2(C_6H_{13}NMe_2)$]	2.005	2.010	144	84	2.407
[$ZnCy_2(C_6H_{13}NMe_2)$]*	2.015	2.018	144	94	2.392

Topological analyses.

Topological methods are based on the analysis of the gradient field of a local function within the dynamic field theory and provide a partition of the molecular space into non-overlapping basins.

The topological analysis of the electron density $\rho(r)$, designed as the Quantum Theory of Atoms in Molecules (QTAIM) by R. Bader, yields atomic basins and QTAIM atomic charges.[2] It allows defining bond paths and bond critical points (BCPs). The nature of the chemical bond is characterized from various properties of the electron density at the BCPs, especially the sign of the Laplacian of the electron density and the values of the kinetic energy density (G_{bcp}), of the potential energy density (V_{bcp}) and of the energy density $H_{bcp} = G_{bcp} + V_{bcp}$, following the Bianchi's[3] and Macchi's classification.[4] Negative and positive values for the Laplacian of the electron density at the BCP are assigned to « electron-shared » and « closed-shell » interactions, respectively.[1] Bianchi *et al.*[2] distinguish three bonding regimes, depending on the value of the absolute ratio of the potential energy density to the kinetic energy density ($|V_{bcp}|/G_{bcp}$). The intermediate bond regime ($1 < |V_{bcp}|/G_{bcp} < 2$) lies between electron-shared covalent bonds ($|V_{bcp}|/G_{bcp}$ greater than 2) and closed-shell ionic bonds or van der Waals interactions ($|V_{bcp}|/G_{bcp}$ lower than 1) and includes dative bonds and ionic bonds of weak covalent character. The Macchi's classification relies on the values of both local descriptors and the delocalization index (DI) and offers a way to refine the bond characterization further. The covalence degree may be estimated from the latter and from $|H_{bcp}|/\rho_{bcp}$.[3b] The strength of the interaction may be estimated from the correlation scheme of Espinosa *et al.*[5] providing the corresponding positive interaction energy ($E_{int} = - ½ V_{bcp}$), with E_{int} (kcal mol^{-1}) = -313.754 x V_{bcp} (au)).

The electron localization function (ELF) measures the excess of kinetic energy because the Pauli repulsion.[6] ELF values are confined between 0 and 1. ELF is close to 1 in regions where electrons are single or form antiparallel spin pairs, whereas it tends to 0 in regions where the probability to find parallel spin electrons close to one another is high.[5] ELF tends to 1 in those regions where the electron localization is high (atomic shells. chemical bonds and lone electron pairs),[7] whereas it tends to small values at the boundaries between these regions.[8] The topological analysis of the ELF gradient field yields a partition of the molecular space into non-overlapping electronic domains, basins of attractors, classified into core, valence bonding and nonbonding basins. The attractors, namely local maxima of the ELF function, can be single

points (general case), circles or spheres depending on the symmetry.[9] These basins are in one-to-one correspondence to the core, lone or shared pairs of the Lewis model. A core basin contains a nucleus X (except a proton) and is designated as C(X). A valence bonding basin lies between two or more core basins. Valence basins are further distinguished by their synaptic order, which is the number of core basins with which they share a common boundary. The monosynaptic basins denoted as V(X), correspond to lone pairs, whereas the di- and polysynaptic ones are related to bi- or multi-centric bonds, denoted as V(X1, X2, X3. ...). The average population of the basin is obtained by integration of the one-electron density over the basin volume. A statistical population analysis allows for considering the variance and the covariance of the basin populations, which are related to the electron delocalization.[10] The populations do not take integral values and are about twice the topologically-defined Lewis bond orders for bonding valence basins.[11] The populations and (co)variances of these valence basins can be further interpreted in terms of weighted combinations of mesomeric structures.[6, 11]

Table S4: Relevant QTAIM descriptors (in a.u. except for E_{int} in kcal.mol^{-1}) related to Zn-C and Zn-N bonds in [$ZnCy_2(C_6H_{13}NH_xMe_{2-x})$] complexes (x = 0 - 2). PBE-D3/DGDZVP level of calculation. Bond critical point number. See above for definition and assignment of QTAIM descriptors.

QTAIM molecular graph	BCP	Bond	*V/G*	*-H/ρ*	DI	E_{int}
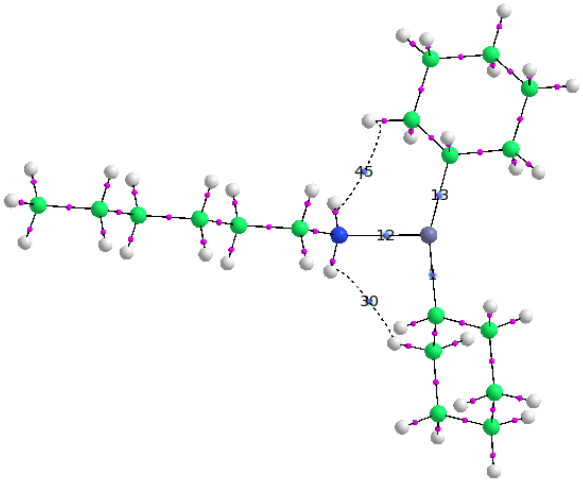	**12**	**Zn-N**	**1.01**	**0.01**	**0.28**	**14.7**
	1	Zn-C	1.49	0.42	0.74	42.0
	13	Zn-C	1.49	0.42	0.75	41.5
	30	H-bond	0.70	-0.22	0.01	0.9
	45	H-bond	0.70	-0.25	0.01	1.3
[$ZnCy_2(C_6H_{13}NH_2)$]						
QTAIM molecular graph	**BCP**	**Bond**	***V/G***	***-H/ρ***	**DI**	**E_{int}**
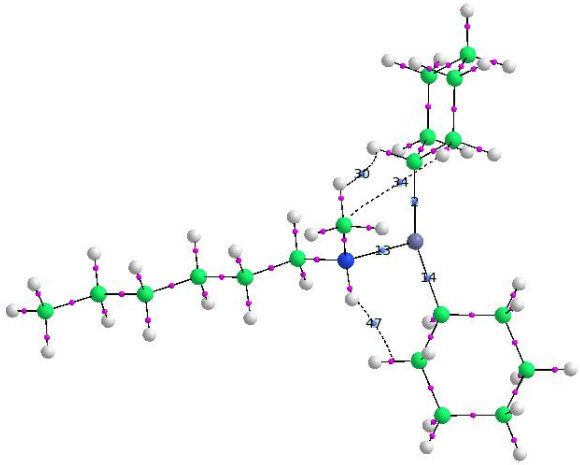	**13**	**Zn-N**	**1.01**	**0.01**	**0.27**	**13.8**
	2	Zn-C	1.49	0.42	0.74	42.1
	14	Zn-C	1.49	0.42	0.74	41.4
	30	H-bond	0.66	-0.25	0.01	0.8
	47	H-bond	0.74	-0.21	0.01	1.5
	34	H-bond	0.63	-0.25	0.01	0.5
[$ZnCy_2(C_6H_{13}NHMe)$]						

QTAIM molecular graph	BCP	Bond	*V/G*	*-H/ρ*	DI	E_{int}
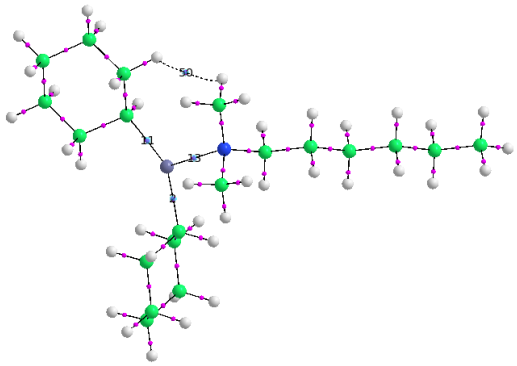	**13**	**Zn-N**	**1.00**	**0.00**	**0.26**	**12.0**
	2	Zn-C	1.48	0.41	0.72	40.9
	11	Zn-C	1.48	0.41	0.75	40.8
	50	H-bond	0.70	-0.22	0.02	1.10
$[ZnCy_2(C_6H_{13}NMe_2)]$						

QTAIM molecular graph	BCP	Bond	*V/G*	*-H/ρ*	DI	E_{int}
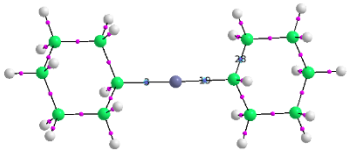	3	Zn-C	1.54	0.44	0.80	43.8
	19	Zn-C	1.54	0.44	0.80	43.8
	28	C-C	4.16	0.79	1.01	73.9
$[ZnCy_2]$						

Table S5: Relevant ELF descriptors of the Zn-C and Zn-N bonds in [$ZnCy_2(C_6H_{13}NH_xMe_{2-x})$] complexes (x = 0 - 2). Descriptors are averaged over both equivalent Zn-C bonds.

	$ZnCy_2$	$[ZnCy_2(C_6H_{13}NH_2)]$	$[ZnCy_2(C_6H_{13}NHMe)]$	$[ZnCy_2(C_6H_{13}NMe_2)]$
V(N)	-	2.17	2.16	2.18
% Zn[a]	-	0.06 (2.8%)	0.06 (2.8%)	0.05 (2.3%)
cov(V(N),C(Zn))	-	-0.08	-0.07	-0.07
V(Zn,C)	2.16	2.12	2.12	2.12
% Zn[b]	0.69 (32%)	0.59 (28%)	0.59 (28%)	0.56 (26%)
Cov(V(Zn,C),C(Zn))	-0.46	-0.36	-0.36	-0.37

a: Atomic contribution of Zn to V(N). b: Atomic contribution of Zn to V(Zn, C)

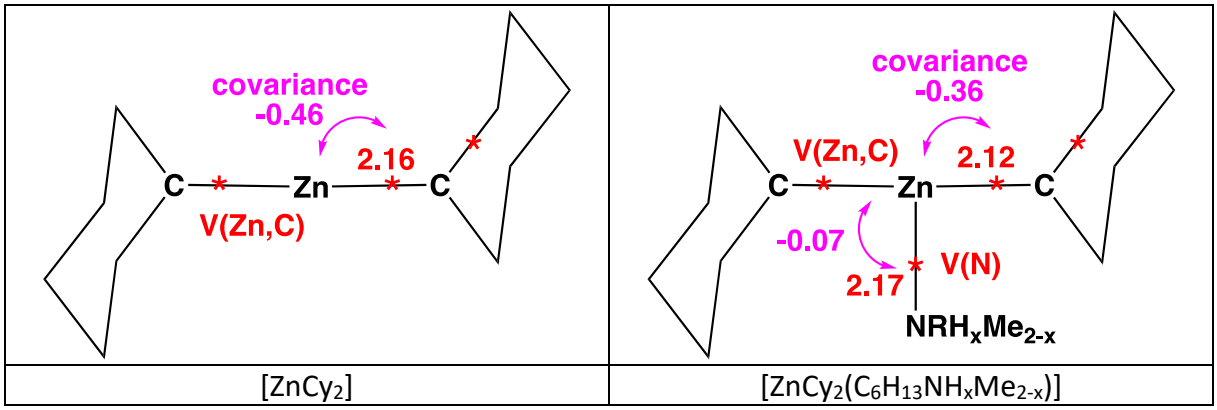

[$ZnCy_2$] | [$ZnCy_2(C_6H_{13}NH_xMe_{2-x})$]

Figure S8: ELF valence attractors and covariances calculated at the PBE-D3/DGDZVP level.

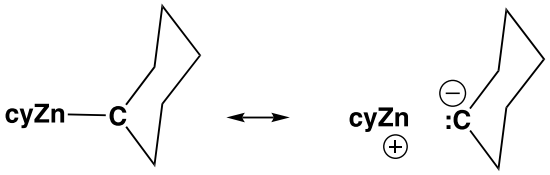

Figure S9: Most representative mesomeric forms of [$ZnCy_2$] from reference 13.

Table S6: Largest values of Fukui indices f_{ELF}^{-} and f_{ELF}^{+} condensed on ELF valence basins of [$ZnCy_2(C_6H_{13}NH_xMe_{2-x})$] complexes (x = 0 - 2). PBE-D3/DGDZVP level of calculation.

f_{ELF}^{-}	$ZnCy_2$	[$ZnCy_2(C_6H_{13}NH_2)$]	[$ZnCy_2(C_6H_{13}NHMe)$]	[$ZnCy_2(C_6H_{13}NMe_2)$]
V(Zn,C)	0.21	0.23	0.23	0.23
V(Zn,C)	0.21	0.21	0.21	0.21
f_{ELF}^{+}	$ZnCy_2$	[$ZnCy_2(C_6H_{13}NH_2)$]	[$ZnCy_2(C_6H_{13}NHMe)$]	[$ZnCy_2(C_6H_{13}NMe_2)$]
V(Zn,C)	0.22	0.08	0.13	0.17
V(Zn,C)	0.22	0.08	0.13	0.11

Table S7: Largest values of Fukui indices f_{QTAIM}^{-} and f_{QTAIM}^{+} condensed on QTAIM basins of [$ZnCy_2(C_6H_{13}NH_xMe_{2-x})$] complexes (x = 0 - 2). PBE-D3/DGDZVP level of calculation.

f_{QTAIM}^{-}	$ZnCy_2$	[$ZnCy_2(C_6H_{13}NH_2)$]	[$ZnCy_2(C_6H_{13}NHMe)$]	[$ZnCy_2(C_6H_{13}NMe_2)$]
C[a]	0.26	0.28	0.29	0.17
C[a]	0.26	0.26	0.25	0.11
f_{QTAIM}^{+}	$ZnCy_2$	[$ZnCy_2(C_6H_{13}NH_2)$]	[$ZnCy_2(C_6H_{13}NHMe)$]	[$ZnCy_2(C_6H_{13}NMe_2)$]
Zn	0.33	0.24	0.14	0.25
N	-	-	0.14	-

a: QTAIM atomic basin of the carbon atom bound to Zn

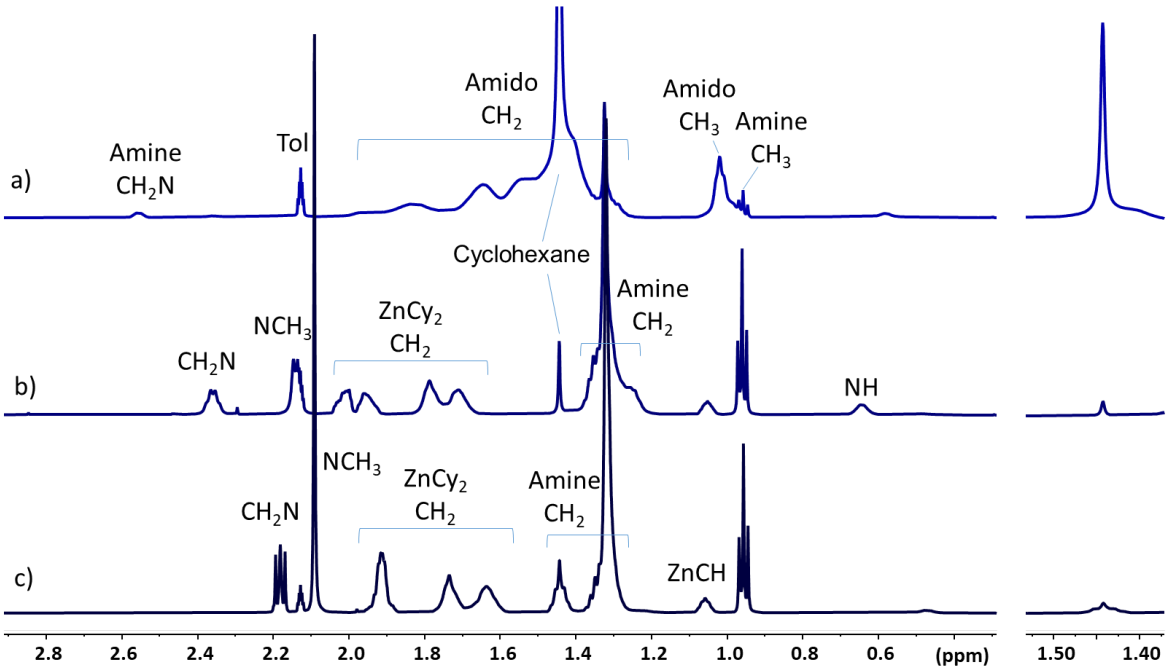

Figure S10: ^{1}H NMR spectra (298 k, Tol-d_8) of $ZnCy_2$ mixed with 2 eq. of C_{12}-NH_2 (after 190 h at 298K- after this delay, the mixture behaves as a gel-[13]) (a), of C_{12}-$NH(CH_3)$ (after 380 h at 298K and 70 h at 323K) (b) and of C_{12}-$N(CH_3)_2$ (after 380 h at 298K and 70 h at 323K) (c). Right enlargement: cyclohexane signal.

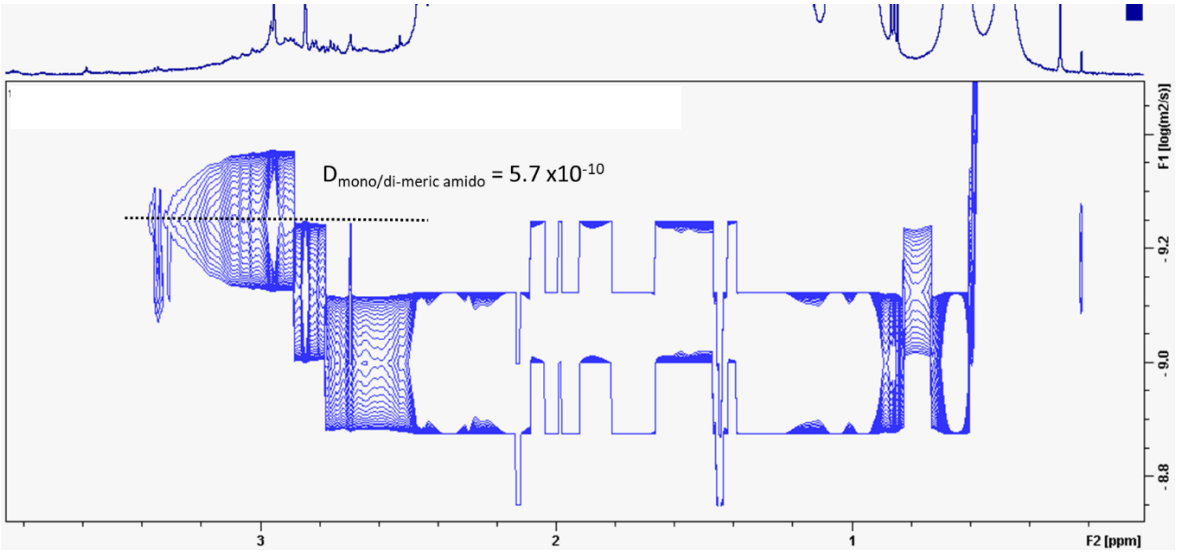

Figure S11: ^{1}H DOSY NMR spectra of [$ZnCy_2$] mixed with 2 eq. of C_{12}-$NH(CH_3)$ after 380 h at 298 K and 70 h at 323 K.

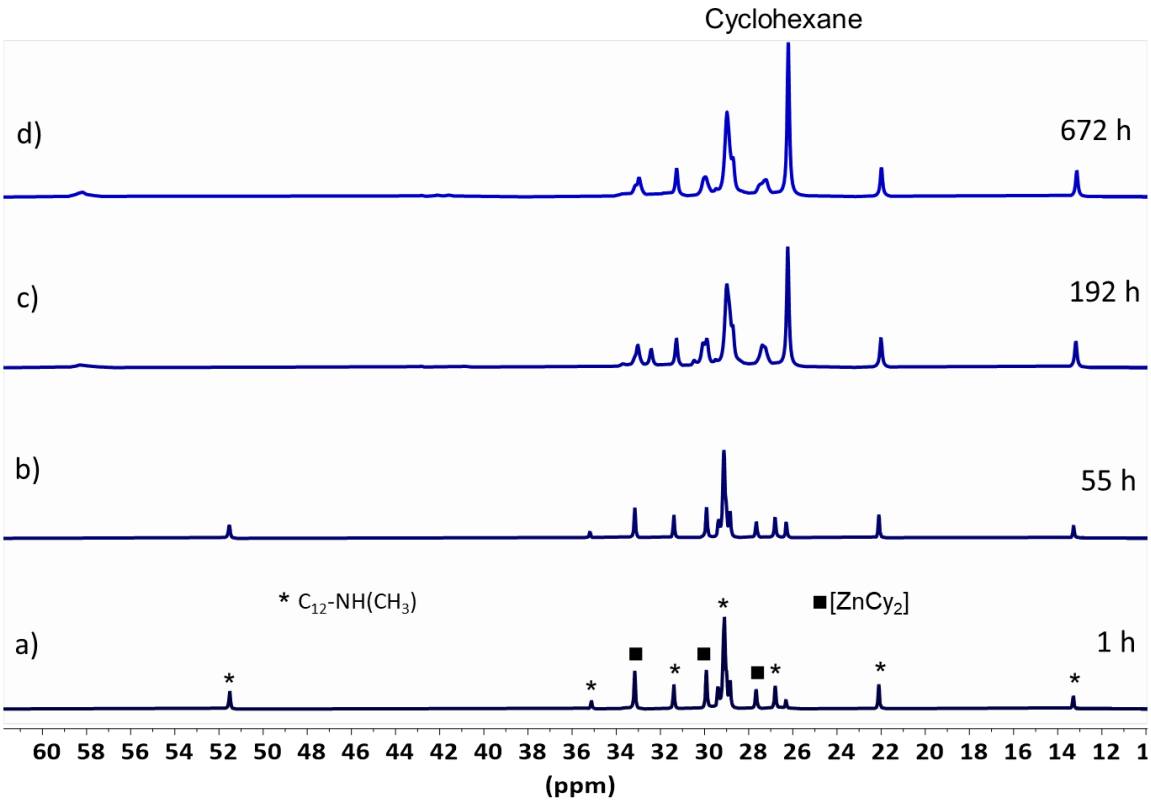

Figure S12: ^{13}C INEPT MAS NMR spectra (295 K) of $ZnCy_2$ with 2 eq. of C_{12}-NH(CH_3) after mixing of 1 h (a). 55 h (b). 8 days (c) and 28 days (d).

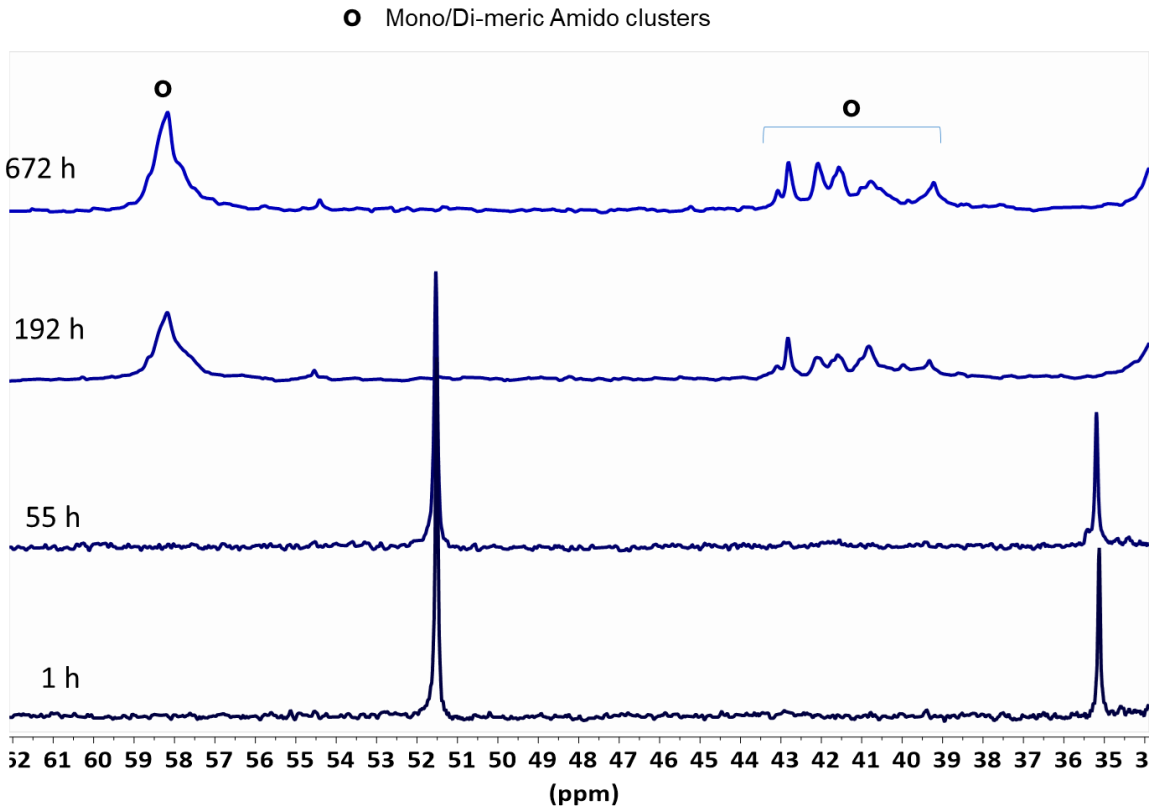

Figure S13: Enlargement of ^{13}C INEPT MAS NMR spectra (295 K) of $ZnCy_2$ with 2 eq. of C_{12}-$NH(CH_3)$ after mixing of 1 h (a). 55 h (b). 8 days (c) and 28 days (d).

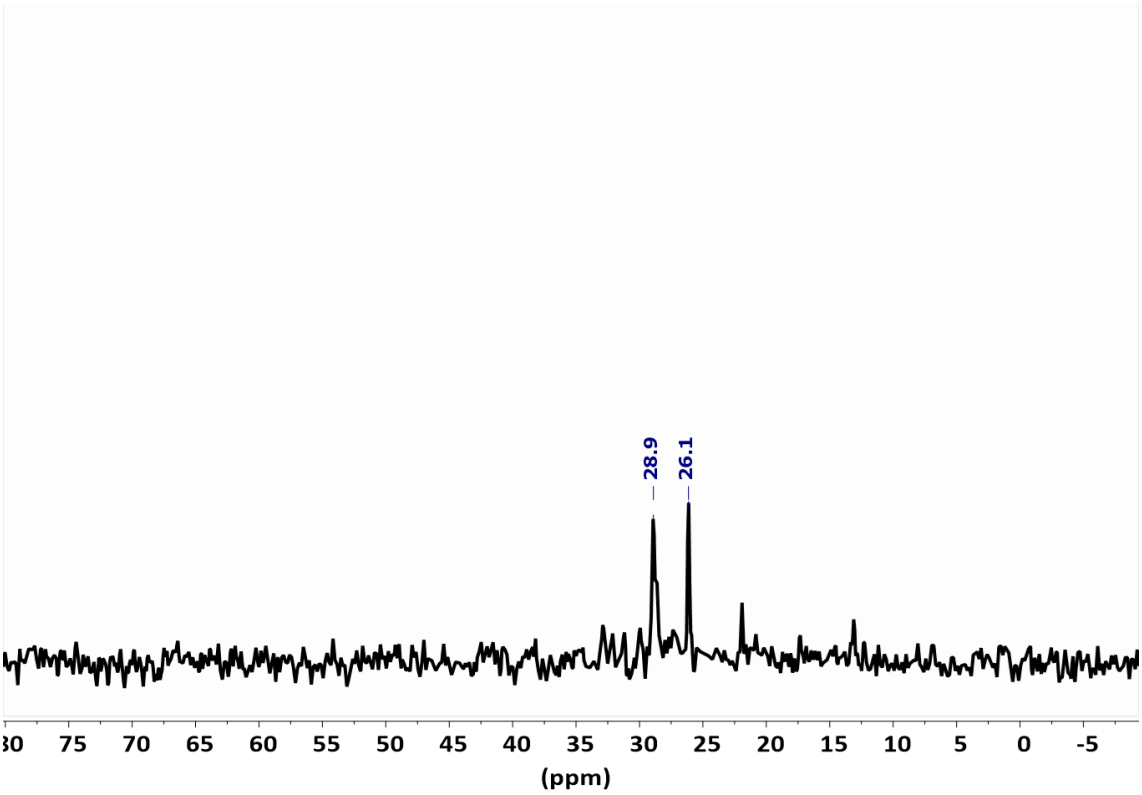

Figure S14: ^{13}C CPMAS NMR spectrum (295 K) of $ZnCy_2$ with 2 eq. of C_{12}-$NH(CH_3)$ after mixing of 28 days.

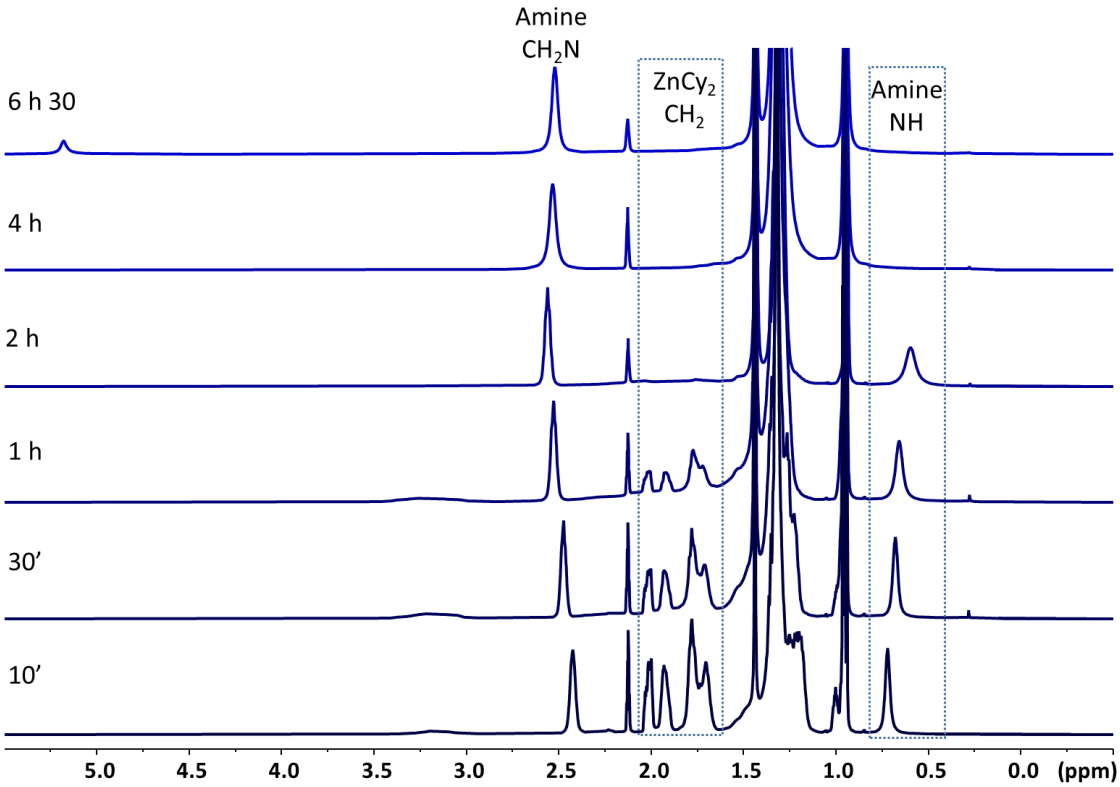

Figure S15: ^{1}H NMR spectra (298 °K, toluene-d_8) of $ZnCy_2$ mixed with 2 eq. of C_{12}-NH_2 after different hydrolysis reaction times.

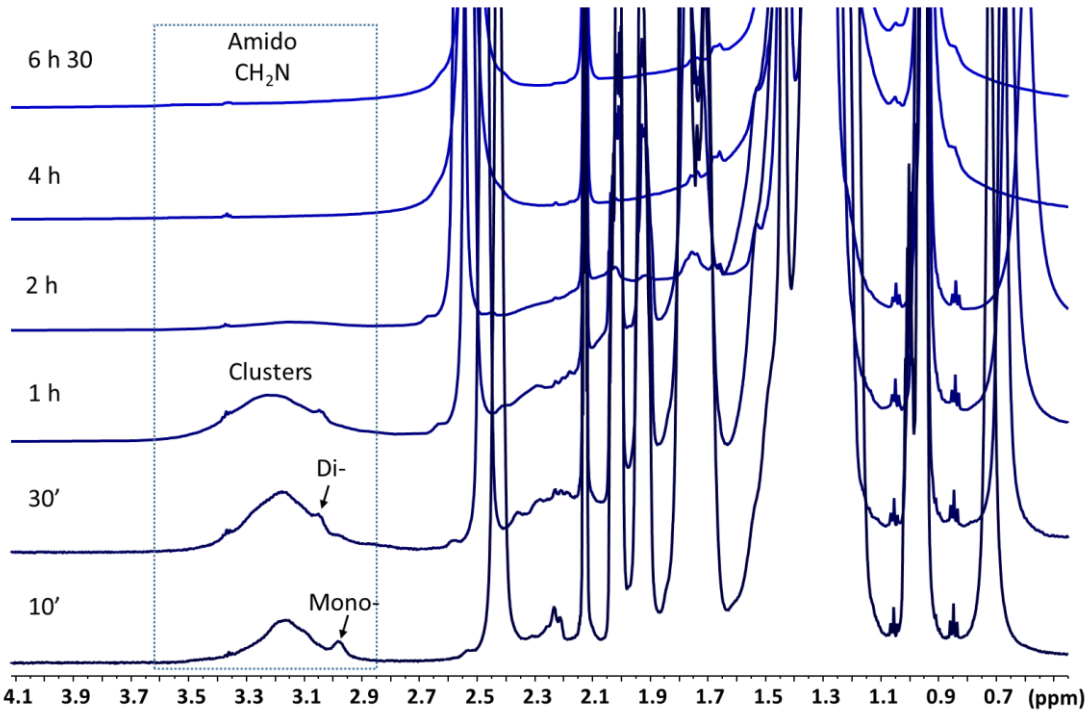

Figure S16: vertical enhancement of the ^{1}H NMR spectra (298 °K, toluene-d_8) of $ZnCy_2$ mixed with 2 eq. of C_{12}-NH_2 after different hydrolysis reaction times presented Figure S14.

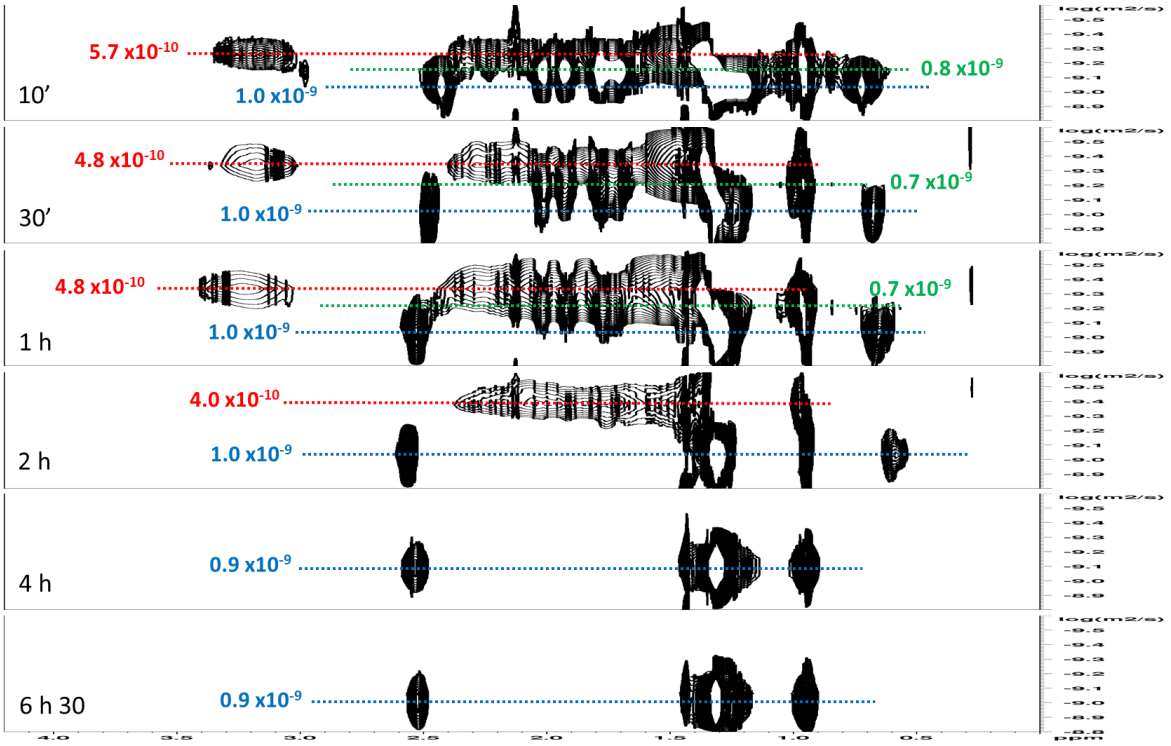

Figure S17: ^{1}H DOSY NMR spectra (298 °K, toluene-d_8) of $ZnCy_2$ mixed with 2 eq. of C_{12}-NH_2 after different hydrolysis reaction times.

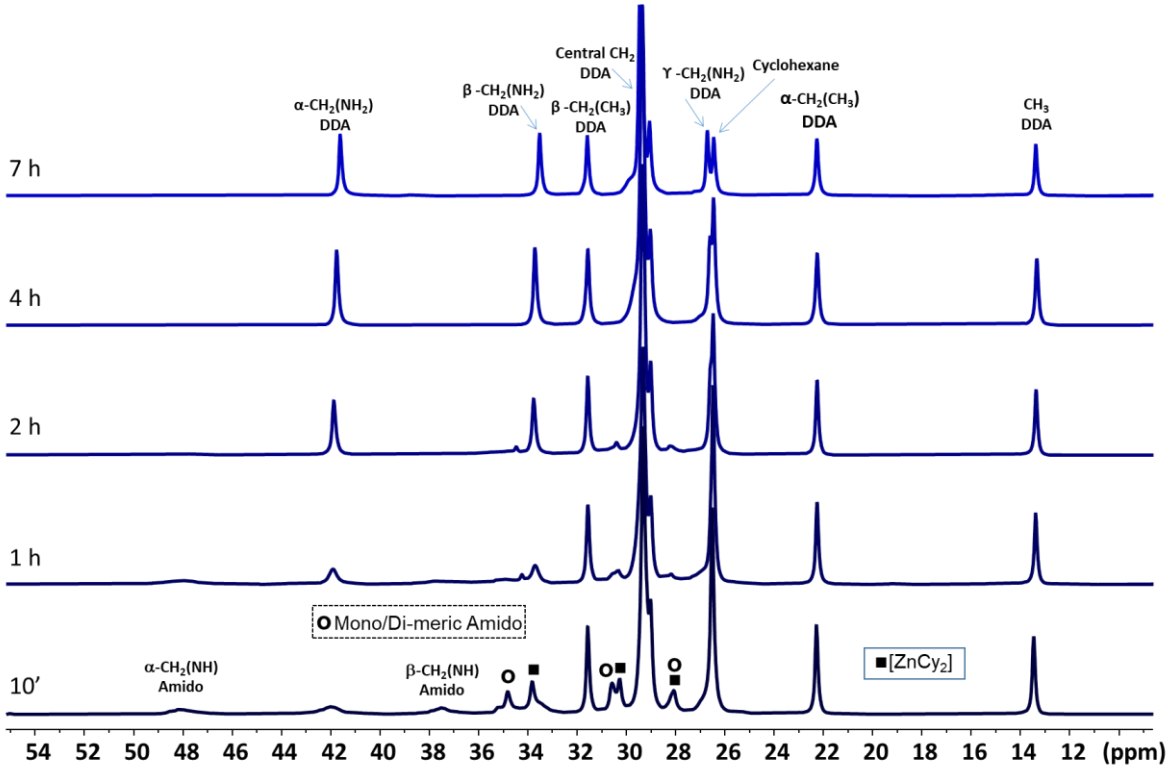

Figure S18: ^{13}C INEPT MAS NMR spectra (295 °K) of $ZnCy_2$ with 2 eq. of C_{12}-NH_2 under water vapor with mixing times.

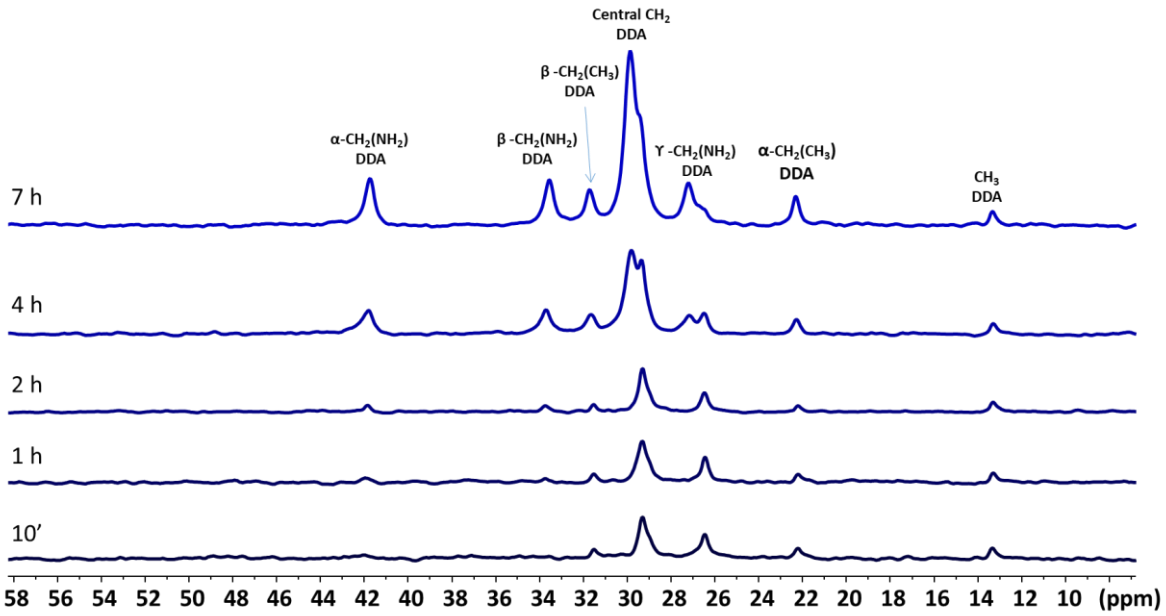

Figure S19: ^{13}C CP MAS NMR spectra (295 K) of $ZnCy_2$ with 2 eq. of C_{12}-NH_2 under water vapor with mixing times

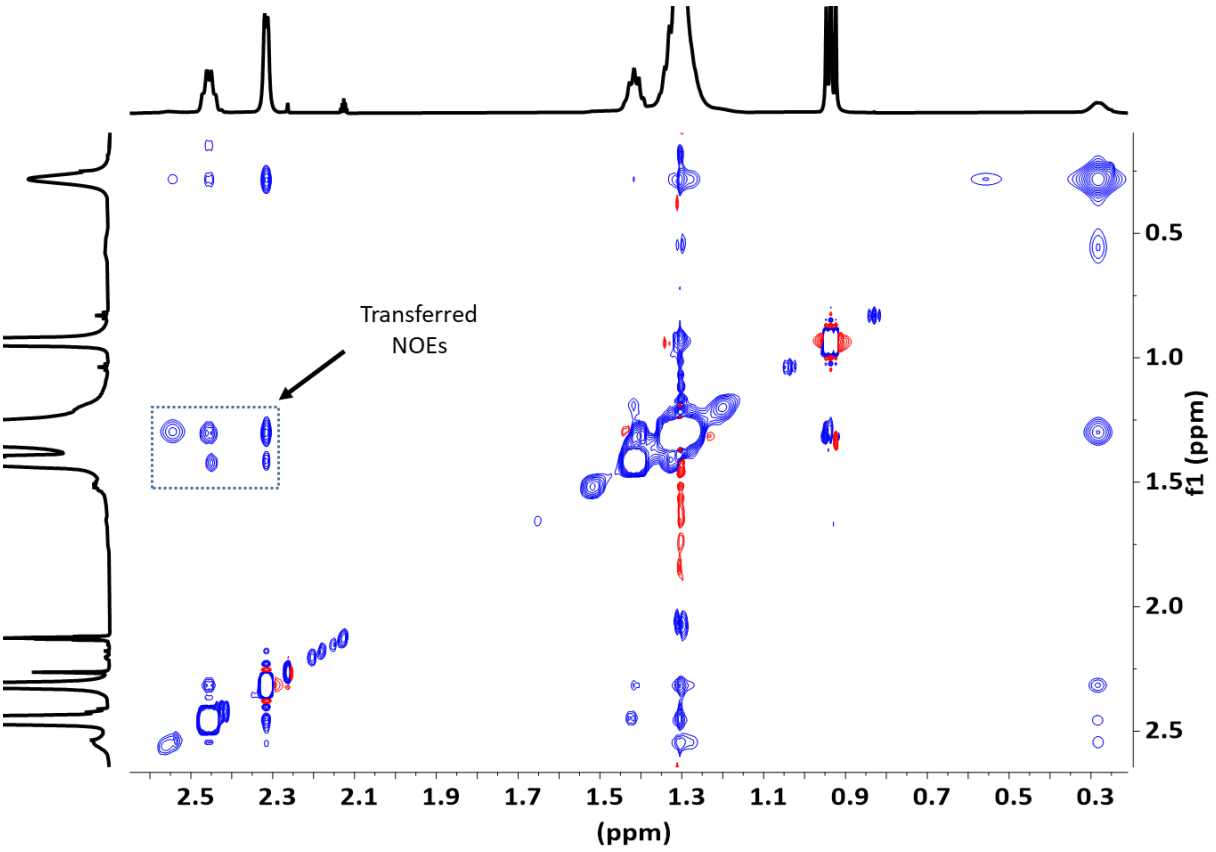

Figure S20: ^{1}H NOESY NMR spectra of ZnO with 1 eq. of C_{12}-NH_2 and 10 eq. of C_{12}-$NH(CH_3)$.

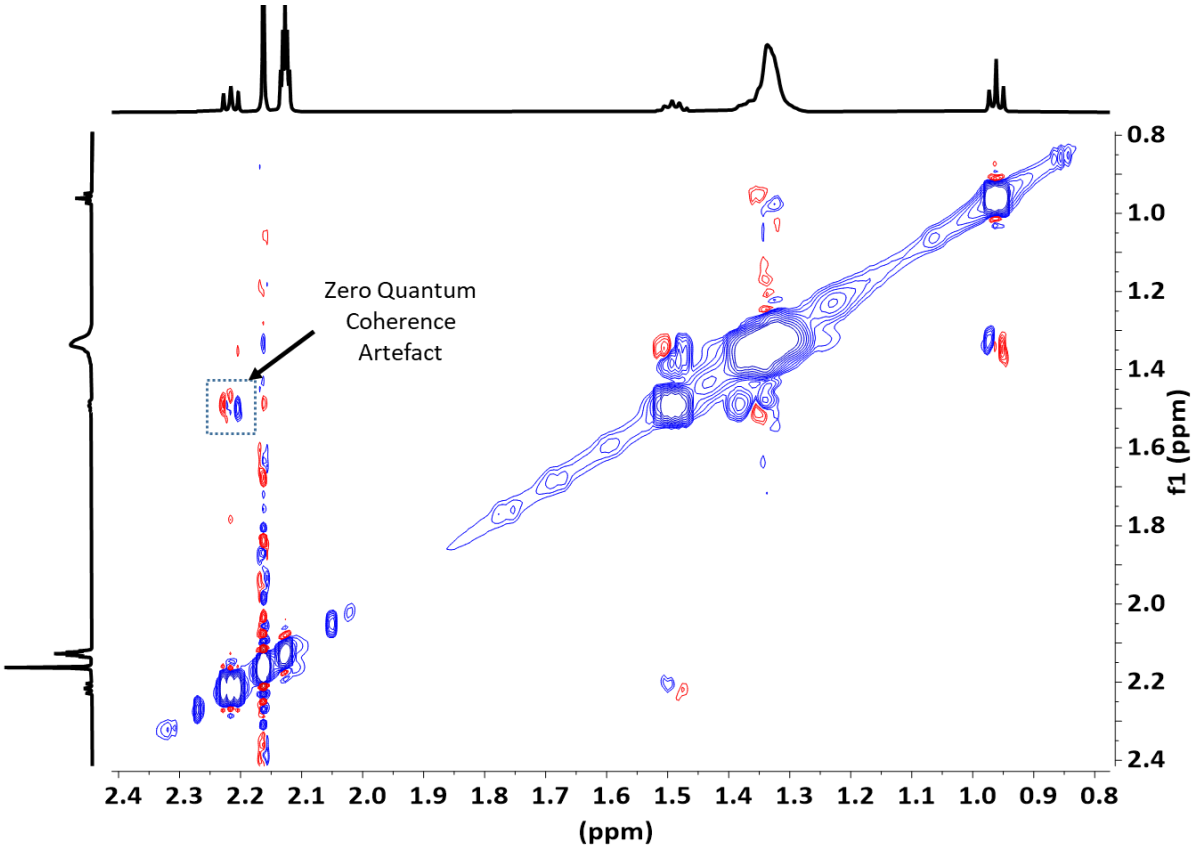

Figure S21: ^{1}H NOESY NMR spectra of ZnO with x eq. of C_{12}-N$(CH_3)_2$

1- Zheng, Z.; Butynska, R.; Valverde Serrano, C.; Marty, J.-D.; Mingotaud, C.; Kahn, M. L. *Chem. Eur. J.*, **2016**, *22*, 15614-15618.
2- M. L. Kahn, M. Monge, V. Collière, F. Senocq, A. Maisonnat, B. Chaudret, *Adv. Func Mater.*, **2005**, *15*, 458-468
2- Bader, R. F. W. *Atoms in molecules*. Clarendon Press: Oxford, 1990.
3- (a) Bianchi, R.; Gervasio, G.; Marabello, D. *Inorg. Chem.* **2000,** *39*, 2360-2366. (b) Espinosa, E. ; Alkorta, I. ; Elguero, J. ; Molins E. *J. Chem. Phys.* **2002**, *117*, 5529-5542.
4- Macchi, P.; Proserpio, D. M.; Sironi, A. *J. Am. Chem. Soc.* **1998,** *120*, 13429-13435.
5- (a) Espinosa, E.; Molins, E. ; Lecomte C. *Chem. Phys. Lett.* **1998**, *285*, 170-173 ; (b) Espinosa, E.; Alkorta, I.; Rozas, I.; Elguero, J.; Molins E. *Chem. Phys. Lett.* **2001**, *336*, 457-461. E_{int} = - ½ V_{bcp} and E_{int} (kcal mol-1) = -313.754 x V_{bcp} (au).
6- Becke, A. D.; Edgecombe K. E. *J. Chem. Phys.* **1990**, *92*, 5379-5403 ; (b) Silvi, B.; Savin A. *Nature* **1994**, *371*, 683–686.
7- Poater, J.; Duran, M.; Sola, M.; Silvi B. *Chem. Rev.* **2005**, *105*, 3911-3947.
8- Silvi. B.; Gillespie, R. J.; Gatti C. **2013**, *9*, 187-226.
9- Silvi, B. ; Fourré, I. ; Alikhani M. E. *Monatshefte für Chemie* **2005**, *136*, 855-879.
10- Silvi B. *Phys. Chem. Chem. Phys.* **2004**, 6, 256-260.
11- (a) Lepetit, C. ; Silvi, B. ; Chauvin R. *J. Phys. Chem. A* **2003**, 107, 464-473 (b) Silvi B. *Phys. Chem. Chem. Phys.* **2004**, *6*, 256-260.
12- Lepetit, C.; Kahn, M. L. *Res. Chem. Int.* **2021**, *47*, 377–395.
13- Zhao, Z. ; Coppel, Y.; Fitremann, J.; Fau, P.; Roux, C.; Lepetit, C.; Lecante, P.; Marty, J.-D.; Mingotaud, C.; Kahn, M. L. *Chem. Mater.,* **2018**, *30*, 8959-8967